راشك

RESEARCH PAPER

Numerical investigation of compact-tension specimen failure based on auxetic structures

Amir Hessam Feizi, Alireza Daneshmehr *

School of Mechanical Engineering, University of Tehran, Tehran, Iran

Abstract

The study of crack growth behavior and fracture mechanisms in engineering materials plays a pivotal role in enhancing the design of resilient structures and in the development of advanced materials. In this context, auxetic structures, characterized by a negative Poisson's ratio, have introduced new perspectives in the field of fracture mechanics due to their unique properties. The present work numerically investigates the fracture behavior of a compact-tension (CT) specimen with a pre-crack and standard geometric dimensions, based on auxetic cellular structures fabricated from 7075-T651 Aluminum Alloy. The objective is to evaluate crack propagation, reaction forces and energy absorption in various lattice structures with negative and positive Poisson's ratios. For this purpose, the specimen geometries were designed by embedding unit cell patterns within the rectangular region of the specimen while maintaining the uniform thickness of the surrounding cell walls. Uniaxial tensile loading was then simulated using pre-designed grips. Furthermore, a uniaxial tensile test simulation was conducted for all specimens in accordance with relevant standards to determine and compare their Poisson's ratios. To facilitate a massindependent comparison of structural performance, the reaction forces were normalized. Analysis of the results indicates that the auxetic structures developed in this study exhibit a significant improvement in fracture resistance over the conventional re-entrant auxetic structure.

Keywords: Auxetic structure; Compact-tension (CT) specimen; FEM; Fracture mechanics; Phase filed

1. Introduction

Fracture mechanics is a fundamental discipline for evaluating the integrity, safety, and durability of engineering components. Understanding crack initiation and propagation is critical not only for predicting service life but also for designing structures with improved resistance to failure. In critical sectors such as aerospace, automotive, and biomedical engineering, the precise control of fracture and fatigue behavior is essential due to stringent operational demands and high safety requirements [1-4]. While traditional studies have focused on homogeneous and composite materials, the advent of mechanical metamaterials (particularly auxetic structures) has created new opportunities to tailor crack growth and improve toughness [5-8].

Auxetic materials are mechanical metamaterials distinguished by a negative Poisson's ratio (NPR). This characteristic causes them to expand transversely when subjected to axial tensile strain, contrary to the lateral contraction observed in conventional solids. This phenomenon was first reported by Lakes in 1987 in re-entrant polyurethane foams [5, 6]. Since then, numerous auxetic topologies, including re-entrant, chiral, anti-chiral, and double-arrowhead designs, have been explored [7, 9]. Foundational contributions include Gibson et al. [10], who in 1982 analyzed the mechanical response of two-dimensional cellular solids, such as re-entrant geometries and

^{*} Corresponding author: daneshmehr@ut.ac.ir

developed predictive equations later confirmed experimentally. Lakes [11] subsequently proposed chiral topologies as potential auxetic forms, while Larsen et al. [12] identified the double-arrowhead geometry, another widely studied auxetic configuration. More recent analytical models have quantified how geometric parameters, such as cell angle and beam length, directly affect the equivalent stiffness and mass in auxetic structures, offering new insights into their vibration and load-bearing behavior [8]. According to Rahimi-Lenji et al. [13], the diversity of auxetic metastructures (AMSs) extends far beyond classical geometries, encompassing star-shaped, arc-shaped, rotating, and origami-based unit cells. Their comprehensive review classifies over 100 auxetic configurations and highlights how geometry-driven anisotropy and non-repetitive unit-cell design can further enhance energy absorption and impact resistance. These studies together established the scientific framework of auxetic mechanics and inspired extensive subsequent research.

The unique deformation mechanisms of auxetics lead to exceptional properties such as enhanced indentation resistance, synclastic curvature, shear stiffness, energy absorption, and fracture toughness [14-18]. These advantages have motivated applications in protective devices, aerospace structures, biomedical implants, and energy-absorbing systems [6, 7]. Recent experiments by Esmaeili et al. [18] on star-shaped auxetic metastructures (STA and STA-DA) further show that these designs can achieve up to 19% higher energy absorption and over 170% higher stiffness under dynamic loading. Experimental and numerical studies consistently confirm the positive impact of auxeticity on fracture performance. For example, Choi et al. [14] reported up to 160% improvement in the fracture toughness of re-entrant metallic foams compared with conventional foams. Similarly, Yang et al. [16] demonstrated more than 200% enhancement in auxetic Kevlar laminates relative to woven composites. Advances in additive manufacturing have further enabled the fabrication of complex auxetic geometries, which have been shown to delay crack initiation and improve energy dissipation [17, 19, 20].

From a fracture mechanics perspective, evaluating stress intensity factors (SIFs), energy release rates, and crack-tip fields in auxetic materials presents distinct challenges. Prawoto et al. [15] showed that although the macroscopic crack-tip field in chiral auxetics resembles that of conventional materials, the plastic zone is significantly influenced by microstructural auxeticity. More recently, Zhang et al. [9] derived asymptotic crack-tip fields for 2D auxetic chiral solids and demonstrated coupled fracture modes induced by microstructural asymmetry. Meanwhile, numerical approaches based on adaptive finite element methods have proven effective for capturing the singular stress field and accurately predicting crack trajectories under linear elastic fracture mechanics [21]. These findings collectively indicate that both microstructural auxeticity and advanced simulation schemes play crucial roles in understanding fracture parameters and the evolution of crack trajectory.

Compact-tension specimens are standard tools in fracture mechanics, providing well-defined stress states and adherence to ASTM standards. Several studies have refined CT analysis, such as Ravi Chandran's [1] net-section mechanics approach for generalized SIF prediction, and Wang et al. [2], who highlighted the limitations of standard solutions in magnesium alloys with crack deflection. Esleman et al. [3] showed that hybrid composites significantly affect CT fracture toughness, while Jabbari et al. [4] demonstrated the use of CT geometries for environment-assisted cracking. Despite these advances, most CT-based studies have focused on conventional or composite materials, leaving the fracture behavior of auxetic and cellular structures relatively underexplored.

Recent efforts have begun to address this gap. Choi et al. [14] and Zouaoui et al. [17] demonstrated that auxetic foams and 3D-printed metallic lattices enhance fracture toughness compared with conventional counterparts. Kolken et al. [19] investigated fatigue crack initiation in auxetic biomaterials, emphasizing microscale mechanisms, while Kramberger et al. [22] combined finite element simulations with experimental validation to examine crack propagation in re-entrant auxetic compact-tension specimens. Their findings confirmed that crack growth is strongly dependent on cell topology and orientation, underscoring the potential of auxetic architectures to guide cracks and prevent catastrophic failure.

In addition to mechanical loading, studies have explored coupled effects such as thermal shock [23], impact resistance [16], and lattice topology optimization [20], reinforcing the multifunctional nature of auxetic structures. Nevertheless, a significant research gap remains: comprehensive comparative fracture analysis of different auxetic geometries (such as re-entrant, double arrowhead, tetrachiral, and anti-tetrachiral) within standardized compact-tension specimens is still lacking, particularly with respect to crack growth behavior, reaction forces, energy absorption, and Poisson's ratio effects in metallic structures.

To bridge this gap, the present study conducts a systematic numerical investigation across cellular structures fabricated from high-strength aluminum alloy 7075-T651 under uniaxial tensile loading. In contrast to earlier works that primarily focused on a re-entrant topology, this research provides a broader comparative basis, offering a more comprehensive evaluation of auxetic and non-auxetic lattices in fracture-dominated applications. The fracture process is simulated using the phase-field damage criterion, enabling quantitative assessment of crack initiation and

propagation based on the critical energy release rate. Furthermore, to ensure objective evaluation, reaction forces were normalized to eliminate mass effects, enabling performance assessment from a lightweight-design perspective that has not been addressed in prior literature.

In this study, the geometries were designed in SolidWorks and analyzed through finite element simulations in COMSOL Multiphysics. The outcomes provide new insights into crack resistance in auxetic CT specimens and identify configurations with superior fracture performance relative to the conventional re-entrant topology.

2. Materials and methods

2.1. Design of auxetic and compact-tension (CT) specimen

The fracture analysis in this study was conducted on compact-tension (CT) specimens. The specimen geometry was designed in accordance with the dimensional requirements stipulated by the ASTM E399-90 standard [24]. A standard compact-tension specimen consists of a single-edge-notched plate with a fatigue pre-crack subjected to tensile loading. The specimen incorporates two holes designed for gripping to apply the load while preventing bending or lateral effects.

The initial geometry was designed in SolidWorks 2024, and the pre-crack modeling was performed in COMSOL Multiphysics 6.2. The specimen thickness (B) was set to 19 mm, and the width-to-thickness ratio (W/B) was determined using Equation (1). Therefore, the width was defined as four times the thickness (W = 4B). The remaining dimensions were calculated according to the aspect ratios of the standard CT specimen, as illustrated in Fig 1.

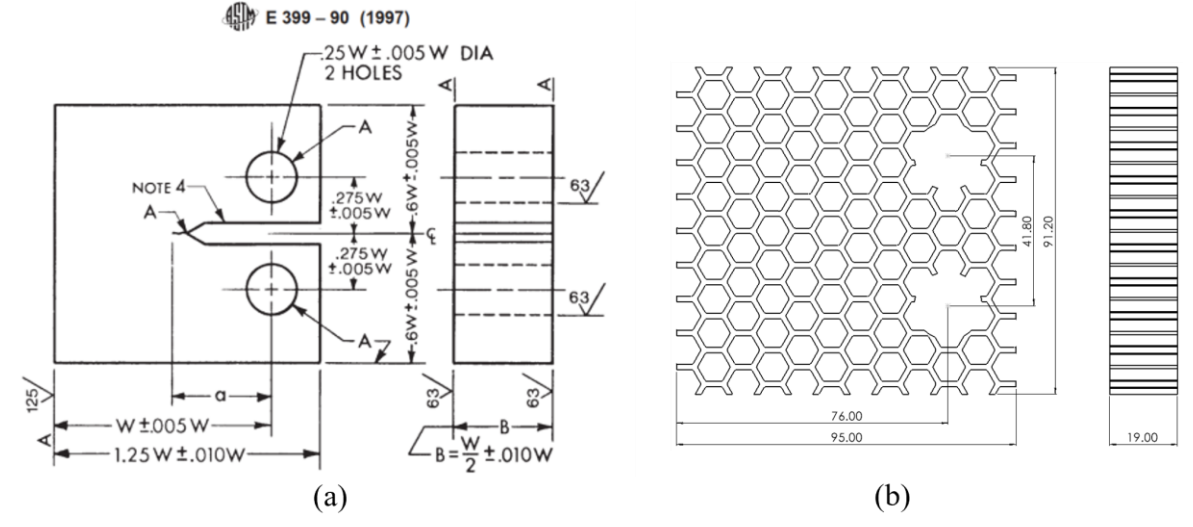


Fig 1. (a) CT specimen geometry in ASTM E399-90 [24] and (b) designed geometry for honeycomb structure

$$\begin{cases} \frac{W}{B} = 2 \text{ for } B > 0.5 \text{ in} \\ \frac{W}{B} = 4 \text{ for } B < 0.5 \text{ in} \end{cases}$$

$$(1)$$

To compare fracture behavior of auxetic structures, one non-auxetic honeycomb structure (used as reference) and four auxetic cellular structures (re-entrant, double-arrowhead, tetrachiral and anti-tetrachiral) were designed. During the design process, cellular structures were created by cutting patterns of unit cells into the rectangular region of the solid compact-tension (CT) specimen, while maintaining a uniform wall thickness of 1.5 mm (Fig 2) for the remaining cellular components.

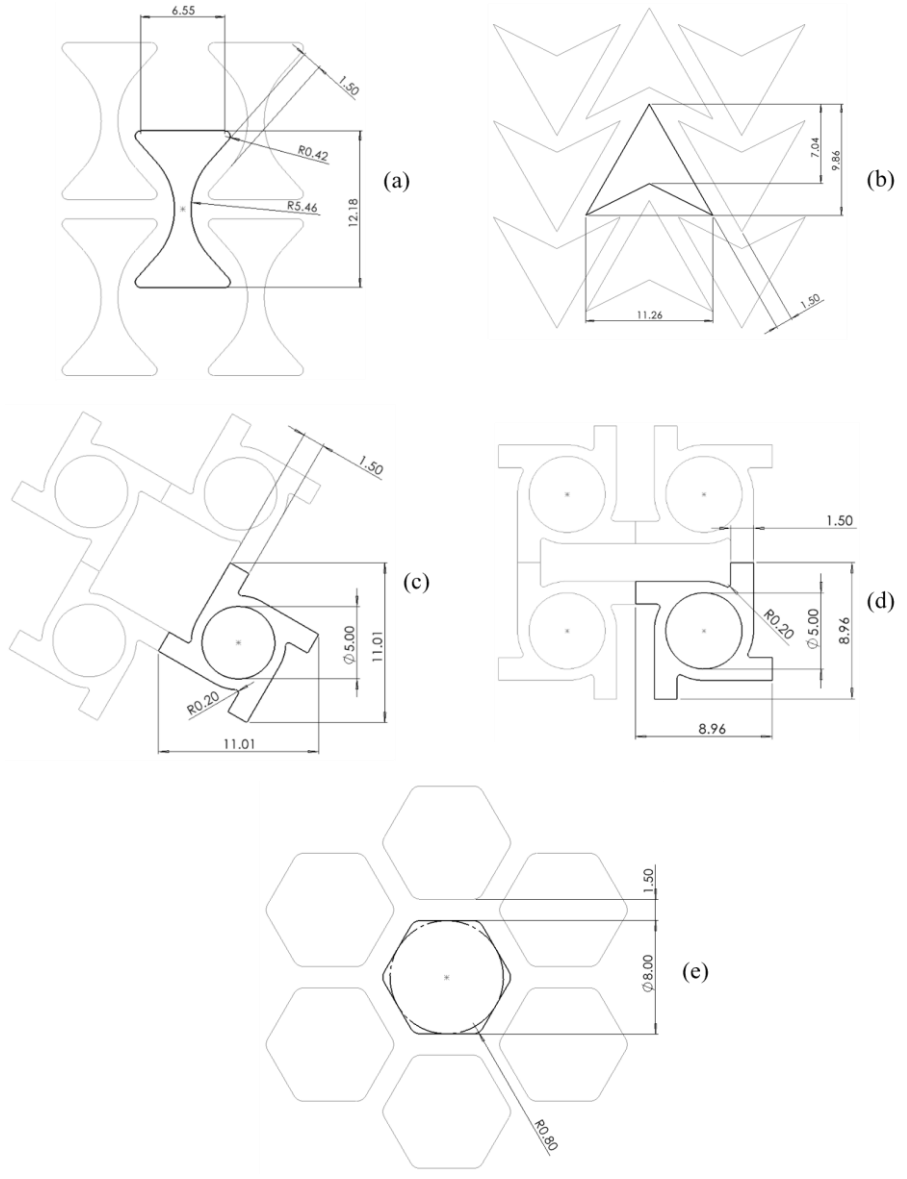


Fig 2. Unit cell dimensions. (a) re-entrant, (b) double-arrowhead, (c) tetrachiral, (d) anti-tetrachiral and (e) honeycomb

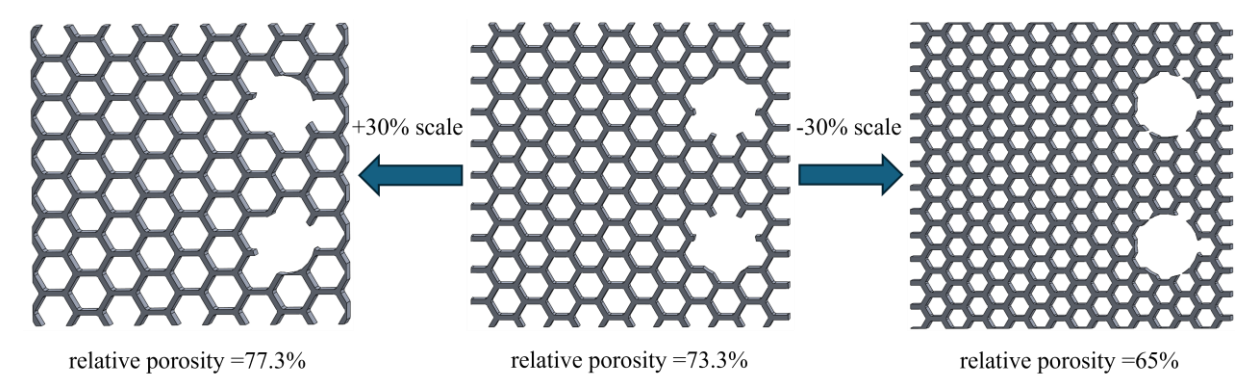


Fig 3. Relative porosity optimization process for honeycomb structure

For a fair comparison, efforts were made to optimize the arrangement of the unit cells to achieve similar relative porosities (defined as the ratio of void volume to total specimen volume) while preserving axial symmetry. Initially, unit cells with equal nominal dimensions were embedded within the compact-tension (CT) specimen, and the

relative porosity was calculated for each design. When a structure exhibited a higher porosity than the target value, the unit-cell scale was reduced and cells were moved closer together to maintain the 1.5 mm wall thickness, thereby increasing the number of cells and decreasing porosity. Conversely, for structures with lower porosity, the unit-cell scale was increased. This iterative adjustment ensured that all models reached comparable relative porosity values, as shown in Fig 3.

To further improve structural performance, curvature was introduced at cell boundaries to reduce stress concentration effects. The final unit-cell geometries are presented in Fig 2, and the corresponding compact-tension (CT) specimens are shown in Fig 4.

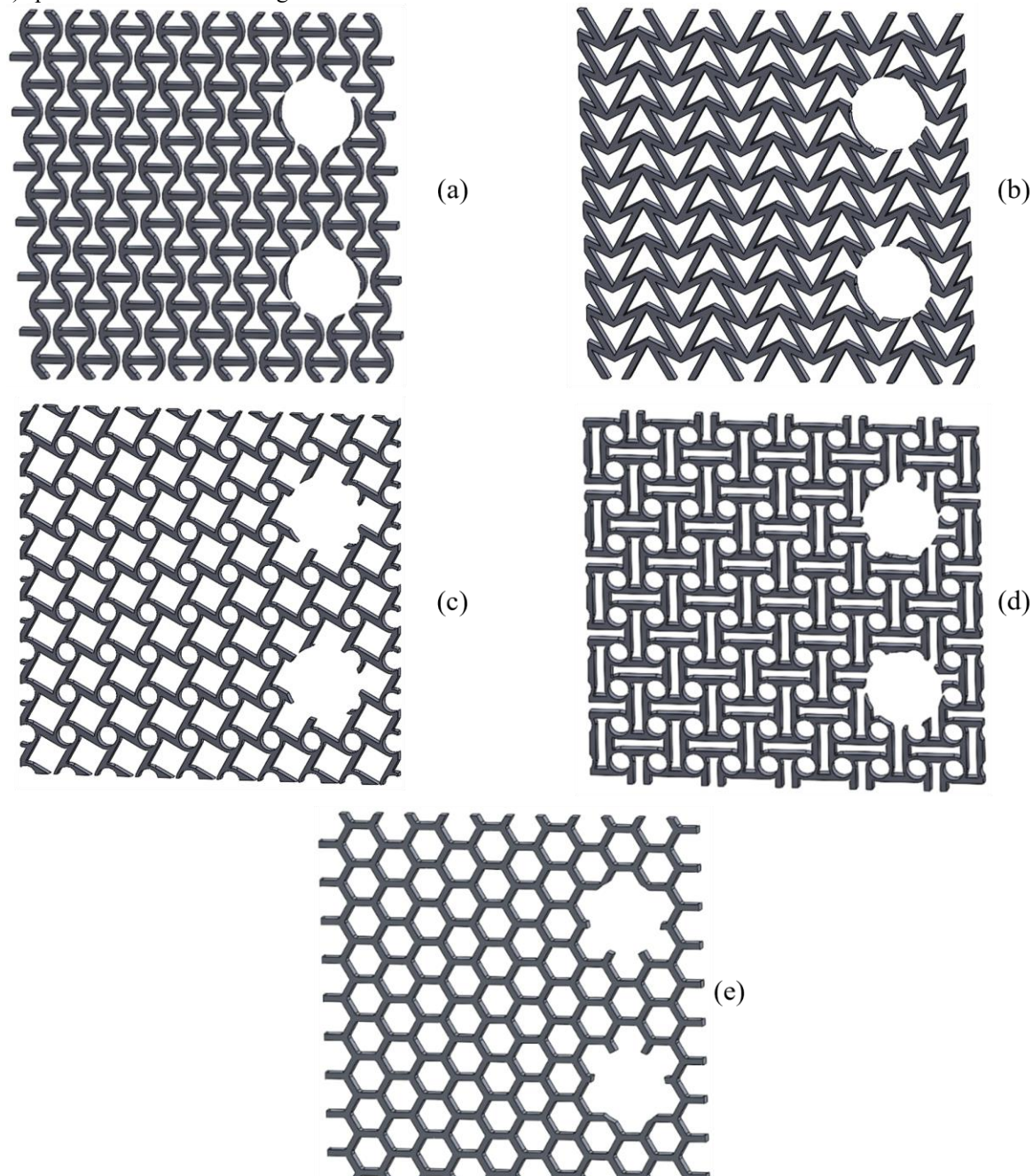


Fig 4. CT specimen cellular structures. (a) re-entrant, (b) double-arrowhead, (c) tetrachiral, (d) anti-tetrachiral and (e) honeycomb

2.2. Materials

The material selected for all specimens was aluminum alloy 7075-T651. This alloy is widely used in aerospace and lightweight structural applications due to its low density, high tensile strength, and favorable fatigue resistance

[25]. These properties make it particularly suitable for fracture analyses and sensitive design applications. The mechanical properties used in the simulations are summarized in Table 1.

Table 1: Mechanical properties of the 7075-T651 Aluminum Alloy at room temperature [2]	2 261

	Mechanical properties					
Materials	Elastic modulus (GPa)	Poisson's ratio	Yield strength (MPa)	Density $(\frac{kg}{m^3})$	Fracture toughness $MPa\sqrt{m}$	
7075-T651 aluminum Alloy	67.199	0.33	498.2	2810	29	

Fig 5 presents the tensile test results of a 7075-T651 aluminum alloy specimen obtained from experimental testing. The specimen was loaded under displacement control, and displacement was measured using a contact extensometer [22]. Based on the results, the material behavior can be approximated as elastic—perfectly plastic.

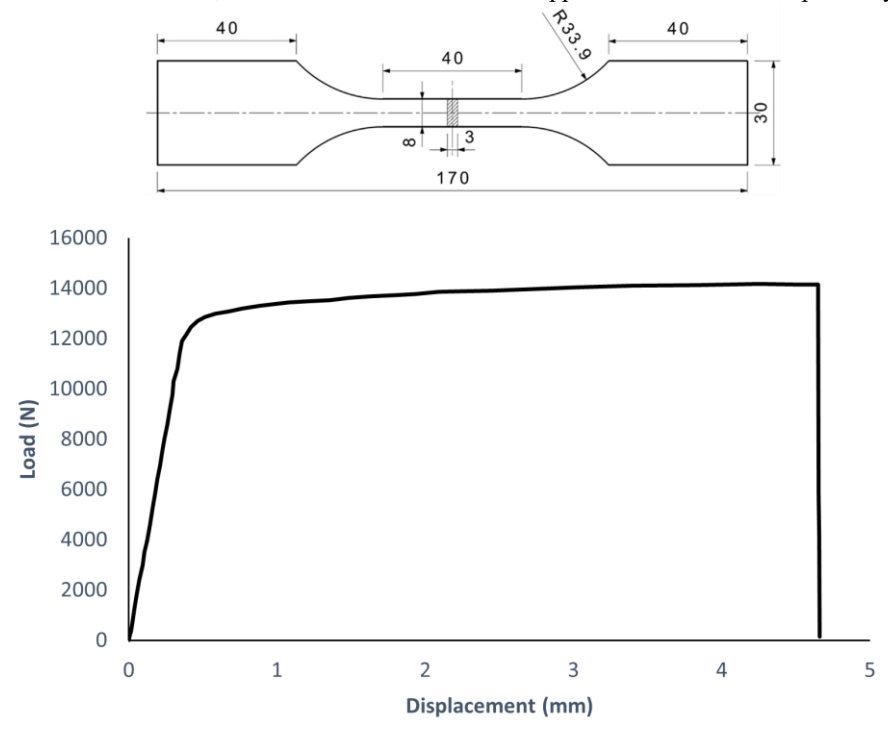


Fig 5. Mechanical response of the 7075-T651 aluminum alloy under tensile loading [22]

2.3. LEFM criterion

Assuming linear elastic material behavior according to Hooke's law, the analysis was performed based on Linear Elastic Fracture Mechanics (LEFM). The validity of this approach requires meeting the conditions specified in Equation (2) [26]:

$$t, a, (b-a), h \ge \frac{4}{\pi} \left(\frac{K_{lc}}{\sigma_y}\right)^2 \tag{2}$$

Where a is the crack length and b is the specimen width. Considering the CT specimen geometry (Fig 1), Equation (2) can be rewritten as:

$$w/4, a, (w-a), 1.2w \ge \frac{4}{\pi} \left(\frac{K_{Ic}}{\sigma_y}\right)^2$$
 (3)

Using the properties in Table 1:

$$K_{Ic} = 29MPa\sqrt{m}, \sigma_y = 498.2MPa$$

$$\Rightarrow \frac{4}{\pi} \left(\frac{K_{Ic}}{\sigma_y}\right)^2 = 4.3mm$$
(4)

Since the pre-crack length (a) in all models was designed to exceed 15 mm, all geometric parameters meet the LEFM validity criterion.

The condition for satisfying the plane strain is defined by Equation (5) [26]:

$$t, a, (b-a), h \ge 2.5 \left(\frac{K_{Ic}}{\sigma_y}\right)^2 \tag{5}$$

Given that the right-hand side of Equation (5) is calculated to be 8.4 mm and all dimensions are greater than this value, the present model also confirms the plane strain condition, in addition to the LEFM approach.

2.4. phase field damage theory

Fracture in brittle or quasi-brittle materials under mechanical loads initiates with elastic deformation. Once the stress or strain exceeds a critical threshold, cracking begins, leading to a non-linear fracture phase following the elastic phase. The nucleation and propagation of cracks are crucial to the material's failure behavior, described by various theories. In continuum damage mechanics, a damage variable is used to represent the extent of crackinduced deterioration, governing the reduction in material stiffness, which establishes a nonlinear stress-strain relationship. Fig 6 shows the stress-strain behavior of a material undergoing damage [27].

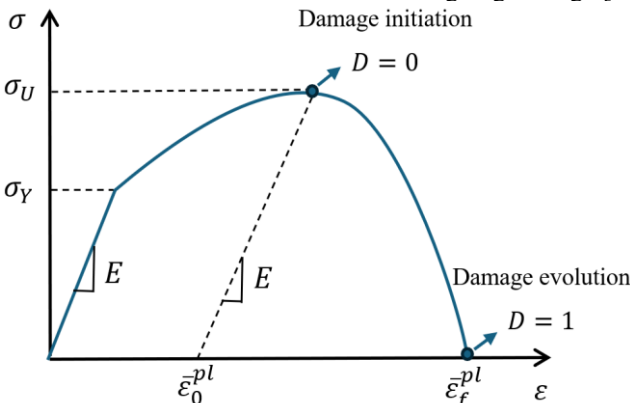


Fig 6. Stress-strain behavior under damage. $\bar{\varepsilon}_0^{pl}$ and $\bar{\varepsilon}_f^{pl}$ are the equivalent plastic strain at the onset of damage and at failure, respectively

The phase-field model is a modern approach for damage analysis that is closely related to strain-based damage models. It enables a precise description of crack initiation and growth, along with its interaction with global structural deformation. The method is derived from the classical Griffith theory, in which the geometric discontinuity of a crack is regularized by introducing a continuous scalar field variable, ϕ , known as the phase field. This variable varies smoothly from $\phi = 0$ in the undamaged (intact) material to $\phi = 1$ in the fully broken region, thereby transforming the sharp crack surface into a diffused damage zone. Incorporating viscous regularization of the crack phase field variable, the governing energy functional for crack propagation is [27, 28]:

$$E(\mathbf{x}, t, \mathbf{u}, \nabla \mathbf{u}, \phi, \nabla \phi) = \int_{\Omega} (1 - d(\phi)) W_{s0} dx + \int_{\Omega} \eta \frac{\partial \phi}{\partial t} dx + \int_{\Omega} G_{c} \left(\frac{1}{2l_{int}} \phi^{2} + \frac{l_{int}}{2} |\nabla \phi|^{2} \right) dx$$
 (6)

where $d(\phi)$ is the damage function, W_{s0} is the elastic strain energy density, η is the viscosity, G_c is the critical energy release rate, and l_{int} is the internal length arising from the regularization of the discrete fracture.

The damage variable in the phase-field model is defined as:

$$d\left(\phi\right) = 1 - \left(1 - \phi\right)^{m} \tag{7}$$

where the exponent m is an adjustable input, commonly set to m = 2.

The crack driving force, $D_{\rm d}$, is a function of the elastic strain energy density and is defined as:

$$D_{\rm d} = \frac{l_{\rm int}}{G_{\rm c} - G_{\rm c0}} \left(W_{\rm s0}^+ - \frac{G_{\rm c0}}{l_{\rm int}} \right) \tag{8}$$

where W_{s0}^+ is the tensile part of the undamaged elastic strain energy density and G_{c0} is an energy threshold introduced to impose an elastic threshold prior to damage initiation [28].

In this study, the phase-field damage model was implemented in COMSOL Multiphysics to simulate crack initiation and propagation in compact-tension (CT) specimens. Crack evolution was governed by the elastic strain energy density, with damage progressing once the accumulated tensile strain energy exceeded the material's resistance, characterized by the critical energy release rate (G_c). The material parameters used for the phase-field simulations are summarized in Table 2.

Table 2: Phase field damage parameters used in this study.					
Critical energy release rate ($\frac{J}{m^2}$)	Length scale (mm)	m [exponent]	Strain energy threshold $(\frac{J}{m^2})$		
12552	0.25	2	0		

2.5. Finite element analysis

The uniaxial tensile loading of compact-tension (CT) specimens was simulated in COMSOL Multiphysics 6.2 using a stationary study, where displacement was gradually increased in increments of 1.25%. Since laboratory loading of CT specimen failure tests is applied slowly and inertia effects are negligible within the studied load range, this analysis was considered sufficient to investigate crack growth behavior.

The pre-crack, as shown in Fig 7, was modeled in the region between the two holes of the specimen. The crack length varied depending on the unit-cell topology but was generally set to correspond to two to three cells, approximately 20 mm in length.

For the boundary conditions, the edges of the top hole were defined as a rigid connector, with displacements restricted at its fixed center in both directions. A prescribed displacement of 12 mm was applied to the center of the bottom hole in the y-direction, while the displacement in the x-direction was constrained to zero. No nonlinear behavior associated with grip contact was introduced into the analysis.

The specimens were meshed using the Free Triangular method (Fig 8), and after conducting a mesh sensitivity analysis, a minimum element size of approximately 0.5 mm was selected. A finer mesh was applied in critical regions, such as the junctions of unit cells, to improve solution accuracy.

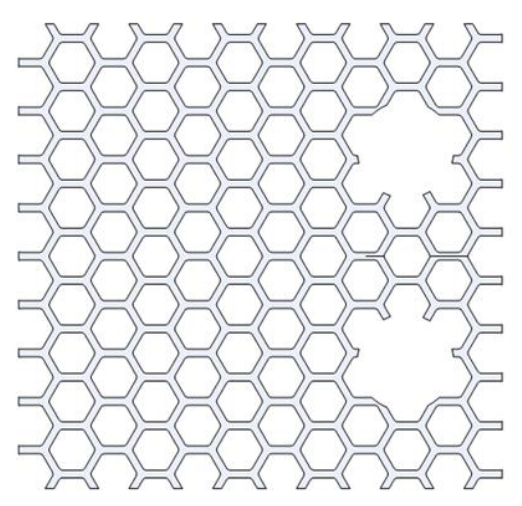


Fig 7. Pre-crack design between two holes for honeycomb sample

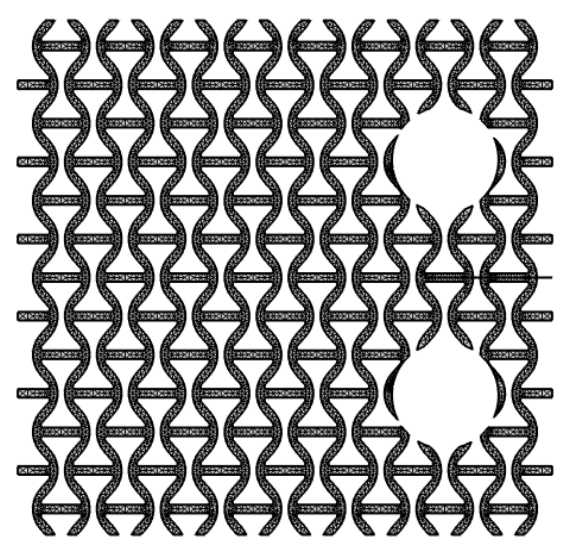


Fig 8. Mesh model of the re-entrant structure

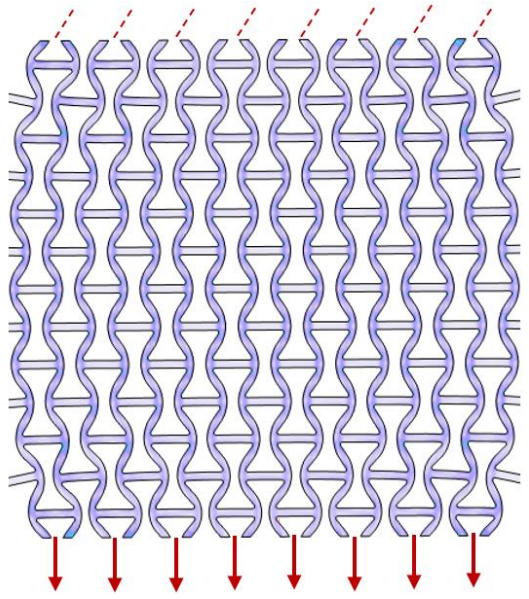


Fig 9. Loading on the re-entrant structure to calculate Poisson's ratio. Scale: 20x

In addition to the fracture test, a separate uniaxial tensile simulation was conducted for all models to calculate Poisson's ratio. In this simulation, the grip holes were removed to maintain loading symmetry. A displacement-controlled load of 0.2 mm was applied at a rate of 5 mm/min (Fig 9). Result validity was confirmed by ensuring that the deformations remained in the elastic range and that the stress did not reach the yield strength. Furthermore, the simulations adhered to ASTM E132-17 [29], which specifies procedures for Poisson's ratio measurement at room temperature.

3. Results and discussion

3.1. Validation of simulation

To validate the simulation methodology and numerical outputs, the cellular geometry introduced in the study by Kramberger et al. [22] was redesigned and simulated under identical loading conditions. While the previous study utilized Abaqus for damage modeling, the current research employed COMSOL Multiphysics, in which the damage modeling criteria and their implementation differ from those of Abaqus. As shown in Figs 10a and 10b, a comparison of the results indicated a difference of 2.3% in the maximum von Mises equivalent stress. Furthermore, the crack propagation paths in both simulations were similar, with only minor differences observed in the stress concentration intensity and local stress distribution.

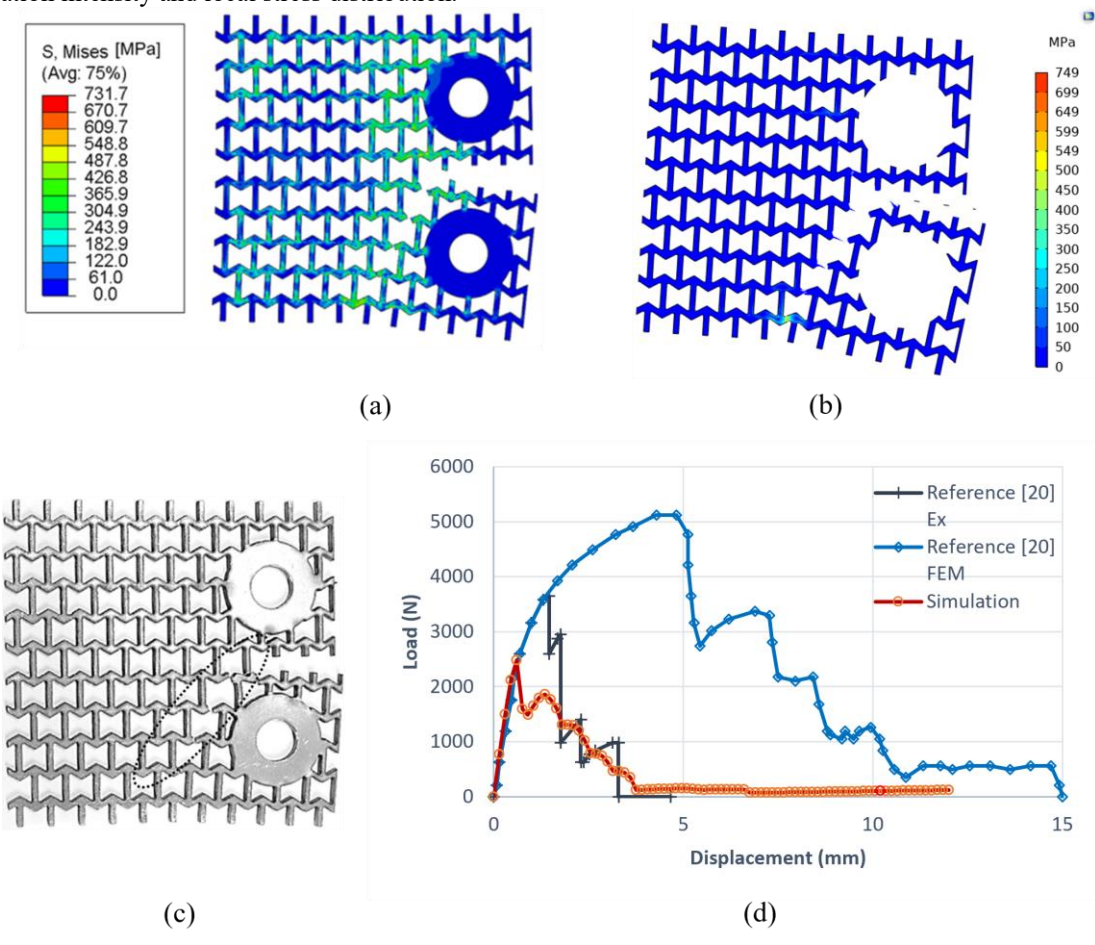


Fig 10. Predicted crack growth from (a) FEM results by Kramberger et al. [22] and (b) the present FEM; (c) experimental results from Kramberger et al. [22]; and (d) comparison of experimental and numerical force-displacement curves from [22] and the present study

As illustrated in Fig 10d, which compares the experimental load-displacement curve with the reference simulation of Kramberger et al. [22] and the present simulation, the current numerical model demonstrates a closer agreement with the experimental reference. The maximum load difference between the experimental test and the

reference numerical simulation was approximately 40.3%, whereas this difference was reduced to 31.9% for the present simulation. Nevertheless, many points along the load-displacement curve exhibit deviations of less than 15%, and several segments following damage initiation match the experimental results. Moreover, the predicted time to complete failure of the cellular structure shows improved accuracy in the current analysis.

This overall consistency highlights the reliability and accuracy of the proposed numerical approach for analyzing the designed geometries.

3.2. Poisson's ratio

Table 5: Poisson's ratio and mass of the investigated structures	d mass of the investigated struc	ctures.
--	----------------------------------	---------

Results	Structures					
	re-entrant	double-arrowhead	tetrachiral	anti-tetrachiral	honeycomb	
Poisson's ratio	-1.12	-0.35	0.31	-0.28	0.44	
Mass (g)	171.57	182.9	119	156.75	123.82	

The results from the uniaxial tensile simulations to determine the Poisson's ratio of the designed structures are presented in Table 3. To calculate the Poisson's ratio, the transverse displacement was obtained from the maximum lateral deformations, which typically occur in the central unit cells, away from the loading and boundary regions.

The honeycomb structure displayed a positive Poisson's ratio, which was the highest among all specimens. Conversely, the re-entrant structure recorded the lowest Poisson's ratio, confirming the most pronounced auxetic behavior and the largest unusual lateral expansion under tension. Despite its relatively high mass, the re-entrant structure exhibited the greatest flexibility and ductility due to the opening behavior of its cells under loading. The designed tetrachiral structure did not exhibit a uniform or symmetrical deformation pattern during the Poisson's ratio simulation, but its average Poisson's ratio was calculated to be positive. Notably, this structure was also the lightest of all specimens investigated, a characteristic of potential significance for lightweight design applications.

3.3. stress and crack trajectory

Since damage evolution occurs at different times across the various cells, a direct comparison of final stress values between structures is not an effective metric for fracture performance. Fig 11 presents the contour plots of the equivalent von Mises stress for two representative cellular structures at the end of loading.

Fracture behavior and crack trajectories for all structures are depicted in Fig 12. A state of complete elemental degradation, enabling its removal from the simulation, is reached when the damage variable attains a value of one.

The simulation results revealed distinct crack propagation patterns. In the honeycomb and double-arrowhead structures, the crack propagation primarily followed the direction of the initial pre-crack, extending almost straight and eventually splitting the specimen into two halves. In contrast, for the re-entrant, tetrachiral, and anti-tetrachiral structures, the crack deviated significantly from its initial path and it extended downward from the side of the hole. This behavior was particularly prominent in the tetrachiral structure, which has an asymmetrical nature; the crack in this structure grew faster and with greater deviation, leaving a larger, relatively intact portion of the specimen. Such crack-guiding capabilities can be beneficial in engineering designs as they allow a larger portion of the cross-section to remain undamaged and prevent catastrophic failure.

For symmetric structures such as the re-entrant and anti-tetrachiral, it was observed that geometric symmetry does not necessarily guarantee straight and symmetric crack growth. Additional factors such as local stress distribution, relative stiffness of cell walls, and unit-cell interactions were found to play decisive roles in guiding the crack path. Generally, it can be concluded that the relative weakness of cell walls oriented in a specific direction creates a preferential path for crack propagation.

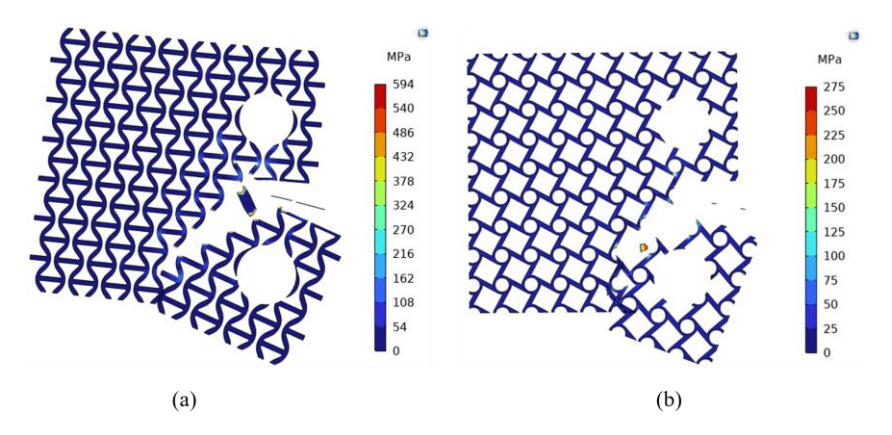


Fig 11. Mises equivalent stress in (a) re-entrant and (b) tetrachiral structures

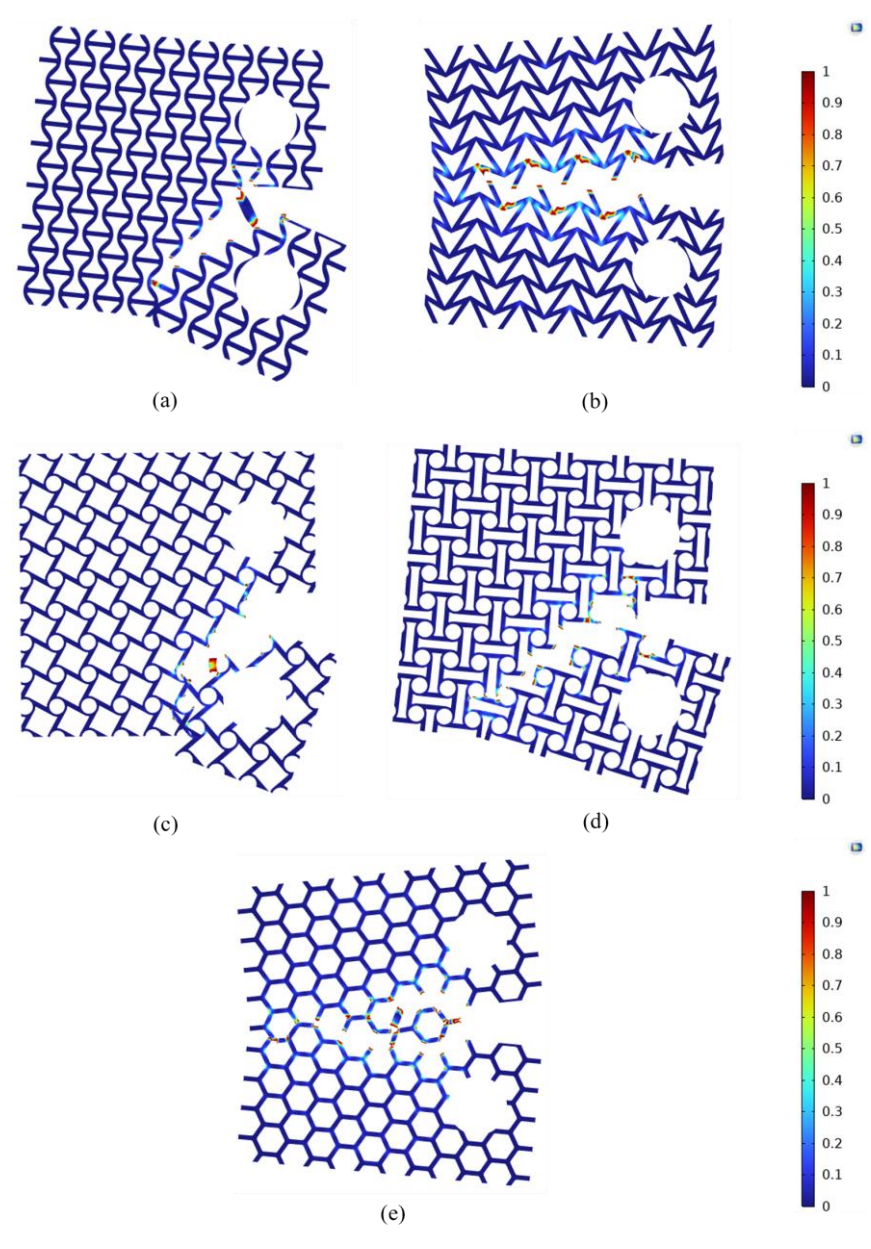


Fig 12. Damage progression in (a) re-entrant, (b) double-arrowhead, (c) tetrachiral, (d) anti-tetrachiral, and (e) honeycomb structures

3.4. load displacement

During the 12 mm loading, the tetrachiral, re-entrant, and honeycomb structures experienced the largest deformations and reached complete failure faster than the other structures. Conversely, the double-arrowhead structure showed the least damage and deformation, indicating its superior resistance to crack propagation. These differences underscore the crucial role of unit cell geometry in governing crack trajectories and determining the overall fracture resistance of cellular structures.

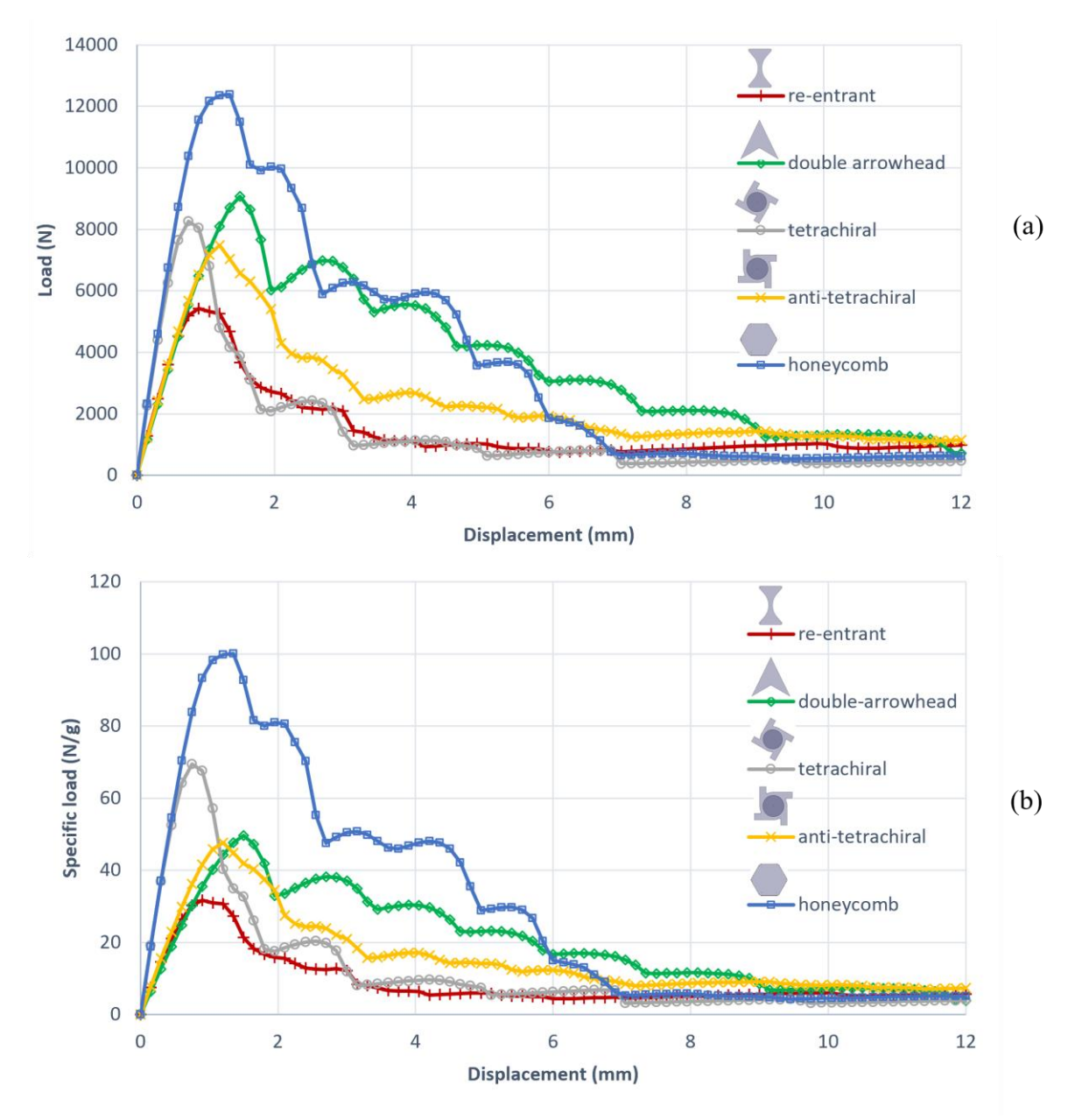


Fig 13. Force-displacement response of cellular structures. (a) Normal form (b) mass-normalized form

Fig 13 exhibits a fully linear trend up to the onset of fracture, with no observable nonlinear deformation or progressive damage in any of the structures. This behavior is indicative of a linear-elastic fracture process at the macroscopic scale and confirms that the assumptions underlying LEFM are satisfied. Moreover, the sudden loss of load-carrying capacity at the damage initiation point reflects a confined plastic zone at the crack tip, consistent with plane-strain behavior. This response contrasts fundamentally with the slow-stable crack growth typically observed under plane-stress conditions.

Analysis of the load-displacement curves in Fig 13 indicates that the maximum and minimum peak reaction forces, both in normal and mass-normalized terms, were recorded for the honeycomb and re-entrant structures, respectively. This behavior is attributable to their mechanical responses: the re-entrant structure, characterized by its lowest Poisson's ratio and highest flexibility, exhibited significantly reduced stiffness, whereas the honeycomb structure displayed the opposite behavior.

It was observed that in the normal conditions, the double-arrowhead structure sustained a higher load than the tetrachiral structure. However, when the force was normalized relative to mass, the tetrachiral structure demonstrated better force performance. This highlights that for weight-critical applications, normalized metrics are essential for an accurate performance assessment.

From an energy perspective, the results indicate that the honeycomb and double-arrowhead structures recorded the highest absorbed energy, with values of 41.18 J and 39.49 J, respectively. This demonstrates the remarkable fracture energy absorption capability of both the symmetric honeycomb geometry and the specialized double-arrowhead design. In contrast, the re-entrant structure absorbed the least energy (12.41 J), which could be attributed to premature failure and a sudden drop in load-bearing capacity following the degradation of its initial cells.

Overall, these findings highlight the decisive influence of unit cell geometry on the total energy absorption capacity of the cellular structures. A comparison of peak reaction forces and absorbed energies is presented in Fig 14, which clearly illustrates the performance differences among the investigated cellular geometries.

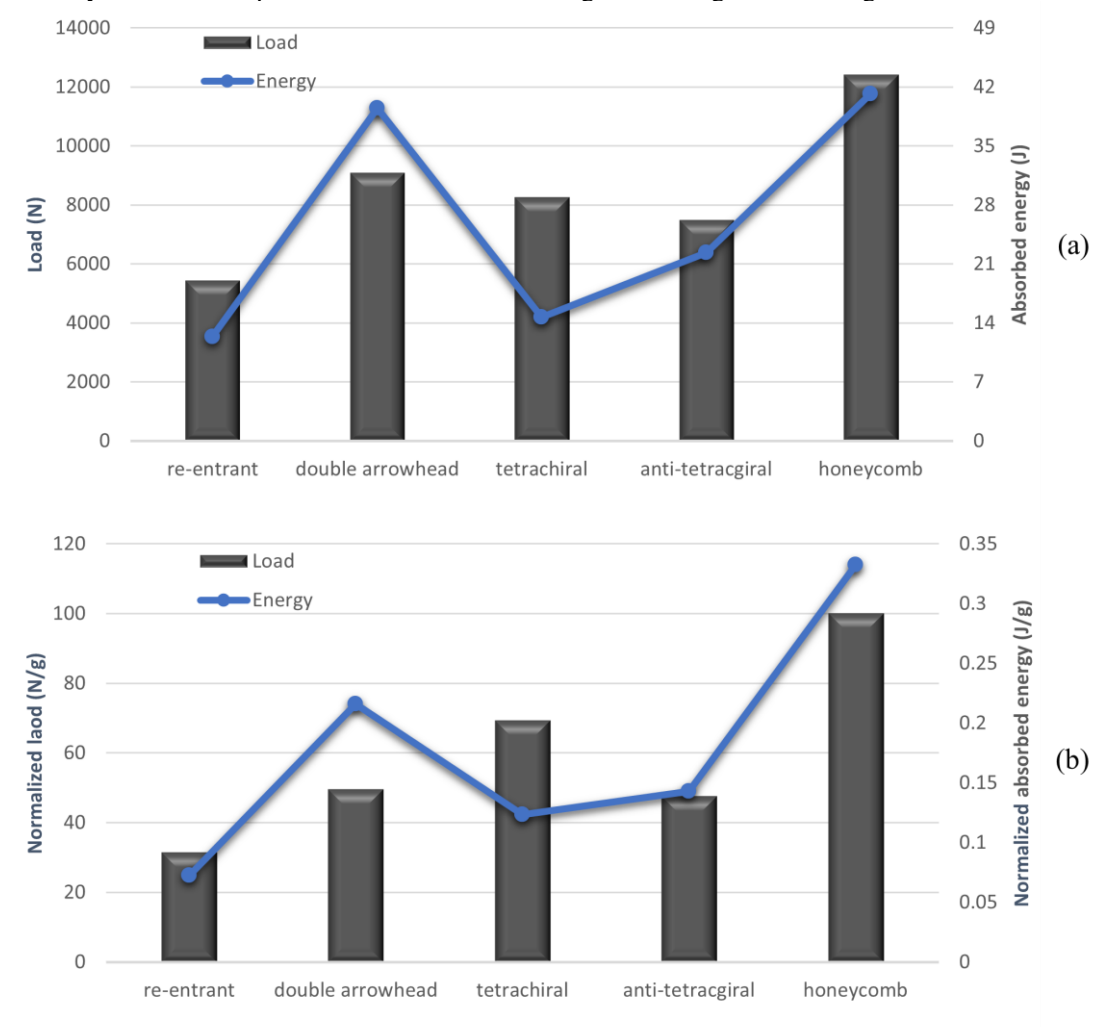


Fig 14. Maximum force and energy absorbed by cellular structures. (a) Normal form (b) mass-normalized form

4. Conclusions

The objective of this study was to investigate the fracture behavior of compact-tension (CT) specimens fabricated from 7075-T651 aluminum alloy featuring both auxetic and non-auxetic cellular structures. For this purpose, five

cellular geometries (honeycomb, re-entrant, double-arrowhead, tetrachiral, and anti-tetrachiral) were designed and analyzed under tensile loading simulations. The influence of these topologies on the effective Poisson's ratio, crack growth trajectory, reaction forces in both normal and mass-normalized terms, and energy absorption was evaluated. The principal findings of this research are summarized as follows:

- Incorporating auxetic geometries significantly altered the effective Poisson's ratio. Specifically, the Poisson's ratio of the base material ($\theta = 0.33$) was reduced to -1.12 in the re-entrant structure, demonstrating a strong auxetic effect.
- Comparison of the damaged geometries revealed the following ranking of fracture resistance, from highest to lowest: double-arrowhead > anti-tetrachiral > honeycomb > re-entrant > tetrachiral. The tetrachiral, re-entrant, and honeycomb structures experienced complete failure at the end of the loading process.
- The maximum reaction force in normal form (12393 N) was calculated in the honeycomb structure, while the minimum peak force (5432 N) was recorded for the re-entrant lattice structure, attributed to its higher ductility and lower stiffness compared with the other structures.
- The mass-normalized analysis showed that structural comparisons based on load-displacement behavior can be mass-dependent. In the normalized form, the superiority of the tetrachiral structure over the double-arrowhead structure became apparent, indicating that mass normalization can lead to different conclusions when lightweight design is a priority.

In summary, the findings of this research demonstrate that auxetic geometries can significantly enhance the fracture performance and energy absorption capacity of structures. These results highlight the potential of auxetic lattices for designing lightweight components and applications that are subjected to cyclic or impact loading. In particular, the ability of auxetic structures to guide and deviate the crack path can play a key role in improving safety and reducing the likelihood of sudden, catastrophic failures in critical components. However, selecting the optimal geometry must be determined by application-specific requirements, including weight, stiffness, and energy absorption capacity.

References

- [1] K. S. Ravi Chandran, Fracture mechanics analysis of generalized compact tension specimen geometry using the mechanics of net-section, *Eng. Fract. Mech.*, Vol. 222, No. 106703, pp. 106703, 2019/12, 2019.
- [2] J. Wang, J. Hu, P. Jin, H. Chen, S. Fu, Z. Liu, H. Gao, X. Wang, X. Chen, Fracture parameters analysis of compact tension specimens with deflected fatigue cracks: ZK60 magnesium alloy, *Theor. Appl. Fract. Mech.*, Vol. 127, No. 104068, pp. 104068, 2023/10, 2023.
- [3] E. A. Esleman, T. Batu, G. Önal, Q. Wu, Investigation of fracture behaviour of hybrid composite materials under compact tension, *Results Eng.*, Vol. 25, No. 104616, pp. 104616, 2025/3, 2025.
- [4] A. H. Jabbari, Z. Silvayeh, P. Auer, J. Stippich, A. Drexler, J. Domitner, Evaluation of environment-assisted cracking using wedge-loaded compact tension specimens, *Procedia Struct. Integr.*, Vol. 68, pp. 874-879, 2025, 2025.
- [5] W. Yang, Z.-M. Li, W. Shi, B.-H. Xie, M.-B. Yang, Review on auxetic materials, *J. Mater. Sci.*, Vol. 39, No. 10, pp. 3269-3279, 2004/5, 2004.
- [6] M. Balan P, J. Mertens A, M. V. A. R. Bahubalendruni, Auxetic mechanical metamaterials and their futuristic developments: A state-of-art review, *Mater. Today Commun.*, Vol. 34, No. 105285, pp. 105285, 2023/3, 2023.
- [7] X. Xue, C. Lin, F. Wu, Z. Li, J. Liao, Lattice structures with negative Poisson's ratio: A review, *Mater. Today Commun.*, Vol. 34, No. 105132, pp. 105132, 2023/3, 2023.
- [8] B. Heidarpour, A. Rahi, M. Shahravi, Analytical modeling and parametric study of equivalent stiffness for auxetic structures, *Journal of Computational Applied Mechanics*, Vol. 54, No. 3, pp. 336-346, 2023. en
- [9] Y. Zhang, H. Yu, S. Zhu, J. Wang, Fracture mechanics analysis of auxetic chiral materials, *Int. J. Mech. Sci.*, Vol. 295, No. 110281, pp. 110281, 2025/6, 2025.
- [10] L. J. Gibson, M. F. Ashby, The mechanics of three-dimensional cellular materials, *Proc. R. Soc. Lond.*, Vol. 382, No. 1782, pp. 43-59, 1982/7/8, 1982.
- [11] R. Lakes, Deformation mechanisms in negative Poisson's ratio materials: structural aspects, *J. Mater. Sci.*, Vol. 26, No. 9, pp. 2287-2292, 1991, 1991.

- [12] U. D. Larsen, O. Signund, S. Bouwsta, Design and fabrication of compliant micromechanisms and structures with negative Poisson's ratio, *J. Microelectromech. Syst.*, Vol. 6, No. 2, pp. 99-106, 1997/6, 1997.
- [13] A. Rahimi-Lenji, M. Heidari-Rarani, M. Mirkhalaf, M. Mirkhalaf, On the internal architecture of lightweight negative Poisson's ratio (auxetic) metastructures: a review, *arXiv preprint arXiv:2505.07385*, 2025.
- [14] J. B. Choi, R. S. Lakes, Fracture toughness of re-entrant foam materials with a negative Poisson's ratio: experiment and analysis, *Int. J. Fract.*, Vol. 80, No. 1, pp. 73-83, 1996, 1996.
- [15] Y. Prawoto, A. Alias, Stress intensity factor and plastic zone of auxetic materials: A fracture mechanics approach to a chiral structure having negative Poisson's ratio, *Mech. Adv. Mater. Struct.*, Vol. 22, No. 3, pp. 213-223, 2015/3/4, 2015.
- [16] S. Yang, V. B. Chalivendra, Y. K. Kim, Fracture and impact characterization of novel auxetic Kevlar®/Epoxy laminated composites, *Compos. Struct.*, Vol. 168, pp. 120-129, 2017/5, 2017.
- [17] M. Zouaoui, O. Saifouni, J. Gardan, A. Makke, N. Recho, J. Kauffmann, Improvement of fracture toughness based on auxetic patterns fabricated by metallic extrusion in 3D printing, *Procedia Struct. Integr.*, Vol. 42, pp. 680-686, 2022, 2022.
- [18] A. Esmaeili, M. Karimi, M. Heidari-Rarani, M. Shojaie, A new design of star auxetic metastructure with enhanced energy-absorption under various loading rates: Experimental and numerical study, *Structures*, Vol. 63, 2024.
- [19] H. M. A. Kolken, A. F. Garcia, A. D. Plessis, A. Meynen, C. Rans, L. Scheys, M. J. Mirzaali, A. A. Zadpoor, Mechanisms of fatigue crack initiation and propagation in auxetic meta-biomaterials, *Acta Biomater.*, Vol. 138, pp. 398-409, 2022/1/15, 2022.
- [20] W. He, W. Luo, J. Zhang, Z. Wang, Investigation on the fracture behavior of octet-truss lattice based on the experiments and numerical simulations, *Theor. Appl. Fract. Mech.*, Vol. 125, No. 103918, pp. 103918, 2023/6, 2023.
- [21] A. Alshoaibi, A two dimensional Simulation of crack propagation using Adaptive Finite Element Analysis, Journal of Computational Applied Mechanics, Vol. 49, No. 2, pp. 335-341, 2018. en
- [22] J. Kramberger, B. Nečemer, S. Glodež, Assessing the cracking behavior of auxetic cellular structures by using both a numerical and an experimental approach, *Theor. Appl. Fract. Mech.*, Vol. 101, pp. 17-24, 2019/6 2019
- [23] J. S. Hu, B. L. Wang, H. Hirakata, K. F. Wang, Thermal shock fracture analysis of auxetic honeycomb layer based on non-Fourier heat conduction, *Engineering Structures*, Vol. 279, No. 115581, pp. 115581, 2023/3, 2023.
- [24] A. International, Standard Test Method for Plane-Strain Fracture Toughness of Metallic Materials, ASTM International, 1990.
- [25] T. Zhao, Y. Jiang, Fatigue of 7075-T651 aluminum alloy, *International Journal of Fatigue*, Vol. 30, No. 5, pp. 834-849, 2008.
- [26] N. E. Dowling, 2012, Mechanical Behavior of Materials, Pearson, Upper Saddle River, NJ, 4thed.
- [27] C. Miehe, M. Hofacker, F. Welschinger, A phase field model for rate-independent crack propagation: Robust algorithmic implementation based on operator splits, *Computer Methods in Applied Mechanics and Engineering*, Vol. 199, No. 45-48, pp. 2765-2778, 2010.
- [28] COMSOL. *Strain-based Damage Models*, Accessed 8 October 2025; https://doc.comsol.com/6.0/doc/com.comsol.help.sme/sme ug theory.06.42.html. English
- [29] A. International, Standard Test Method for Poisson's Ratio at Room Temperature, ASTM International, 2017.